Chemical Science

ROYAL SOCIETY OF CHEMISTRY

EDGE ARTICLE

View Article Online
View Journal | View Issue

Cite this: *Chem. Sci.*, 2024, **15**, 6465

All publication charges for this article have been paid for by the Royal Society of Chemistry

Unravelling the role of spin–vibrational coupling in designing high-performance pentagonal bipyramidal Dy(III) single ion magnets†‡

Sourav Dey, § Tanu Sharma § and Gopalan Rajaraman *

At the cutting edge of high-performance single-molecule magnets (SMMs) lie lanthanide-based complexes, renowned for their potent magnetic anisotropy. SMMs containing one metal centre are defined as single-ion magnets (SIMs). The performance of SMMs is measured generally *via* the barrier height for magnetisation reversal (U_{eff}) and blocking temperature (T_B), below which the magnetisation is fully frozen. To enhance the U_{eff} and T_B values in lanthanide-based SMMs, the static crystal field splitting of m_J levels has been effectively adjusted through ligand design, leveraging the oblate/prolate ground state 4f electron density shape. However, the maximum fine-tuning achievable through ligand design, known as the axial limit, has already been reached in this class of compounds. This necessitates new design principles to enhance SMM characteristics to better suit end-user applications. Among other avenues that can be explored to improve SMM characteristics, a deeper understanding of spin–phonon coupling is critical to advancing T_B values. However, there are only a handful of examples where this has been deciphered. In this work, using a combination of DFT and *ab initio* CASSCF calculations, we have performed spin–phonon calculations on five classes of pentagonal bipyramidal Dy(III) SIMs exhibiting T_B values in the range of 4.5 K to 36 K ([Dy(bbpen)Br] (**1**, H_2bbpen = *N*,*N*′-bis(2-hydroxybenzyl)-*N*,*N*′-bis(2-methylpyridyl)ethylenediamine), $[Dy(OCMe_3)Br(THF)_5][BPh_4]$ (**2**) $[Dy(OSiMe_3)Br(THF)_5]$ $[BPh_4]$ (**3**), $[Dy(L^{N5})(Ph_3SiO)_2](BPh_4)\cdot CH_2Cl_2$ (**4**) and $[L_2Dy(H_2O)_5][I]_3\cdot L_2\cdot H_2O$ (**5**, L = ^{t}BuPO(NH^{i}Pr)$_2$)). Unlike the method employed elsewhere for the calculation of spin–phonon coupling, in this work, we have employed a set of criteria and intuitively selected vibrational modes to perform the spin–phonon coupling analysis. The approach provided here not only reduces the computational cost significantly but also suggests chemical intuition to improve the performance of this class of compounds. Our calculations reveal that low-energy vibrational modes govern the magnetisation relaxation in these SIMs. A flexible first coordination sphere found on some of the complexes was found to be responsible for low-energy vibrations that flip the magnetisation, reducing the T_B values drastically (complexes **2** and **3**). On the other hand, a rigid first coordination sphere and a stiff ligand framework move the spin–vibrational coupling that causes the relaxation to lie beyond the secondary coordination sphere, resulting in an increase in T_B values. Our calculations also reveal that not only the atoms in the first coordination sphere but also those in the secondary coordination sphere affect the performance of the SMMs. Learning from this exercise, we have undertaken several *in silico* models based on these vibrations to improve the T_B values. Some of these predictions were correlated with literature precedents, offering confidence in the methodology employed. To this end, our comprehensive investigation, involving twenty-three molecules/models and five sets of geometries for pentagonal bipyramidal Dy(III) single-ion magnets (SIMs), unveils a treasure trove of chemically sound design clues, poised to enhance the T_B values in this fascinating molecular realm.

Received 2nd February 2024
Accepted 22nd March 2024

DOI: 10.1039/d4sc00823e

rsc.li/chemical-science

Department of Chemistry, Indian Institute of Technology Bombay, Powai 400076, Mumbai, India. E-mail: rajaraman@chem.iitb.ac.in

† Dedicated to the 60th birthday of Prof. R. Murugavel.

‡ Electronic supplementary information (ESI) available: This contains structural parameters in optimised *versus* crystal structures, tables containing *ab initio* calculated parameters, additional figures, optimised geometries, frequencies of the various normal modes of vibrations, computed crystal field parameters, and optimised coordinates of the complexes. See DOI: https://doi.org/10.1039/d4sc00823e

§ Both authors contributed equally to this manuscript.

1. Introduction

Single-molecule magnets (SMMs) are nanoscale molecule-based magnets exhibiting permanent magnetisation similar to bulk magnets, opening up the bottom-up approach to molecule-based devices such as the new generation of information storage devices, solid-state Q-bits for quantum computing and spintronics devices. However, to employ these molecules in end-user applications, magnetic relaxation time (τ), the time-scale in which an SMM preserves its magnetisation, and blocking temperature (T_B) below which the magnetisation is fully frozen need to be improved.[1–9] Furthermore, the molecule should be stable under ambient conditions for the fabrication process to realise the potential applications proposed. While early SMMs based on transition metal clusters yielded T_B values in the range of liquid helium temperatures, the advent of lanthanide-based SMMs significantly improved T_B values.[10–12] The first mononuclear lanthanide-based SMM, $[TbPc_2]^-$ (Pc = phthalocyanine), was discovered in 2003 and is reported to have a T_B value of 1.7 K and U_{eff} of 230 cm^{-1}.[13] Thereafter, many lanthanide-based SMMs have been reported until 2015, but the T_B value did not reach beyond 5–8 K despite having a very large U_{eff} value.[13–34] The breakthrough in lanthanide-based SIMs was achieved in 2016 when a pentagonal bipyramidal $[L_2Dy(H_2O)_5][I]_3\cdot L_2\cdot H_2O$ (L = $^tBuPO(NH^iPr)_2$) molecule was reported with a T_B value of 12 K (based on zero-field cooled/field cooled (ZFC/FC)) by some of us,[35] and at the same time several pentagonal bipyramidal family molecules were also reported by others with slightly larger T_B values.[35–38] We have further demonstrated the role of weak equatorial and strong axial ligand fields in designing high-performance SIMs with very large U_{eff} and T_B values. This is followed by several pseudo pentagonal bipyramidal complexes in the literature where U_{eff} and T_B values reached as high as 1800 K and 36 K, respectively.[36,37,39–45] Later years witnessed a tremendous increase in T_B values by a class of SIMs commonly called dysprosocenium class of molecules having T_B values as high as 80 K – although this class of molecules lacks ambient stability posing further challenges in taking these molecules to end-user applications.[46,47]

The magnetisation relaxation of a SIM occurs *via* quantum tunnelling of magnetisation (QTM) at very low temperatures due to the low-symmetry component of the crystal field (CF).[12] At higher temperatures, it occurs through various spin–vibrational couplings such as direct, Raman and Orbach pathways.[12] The direct process is a barrier-less process which involves a direct transition from the "up" to the "down" spin state, where the crystal lattice absorbs the energy released by the spin system.[12] The Orbach process is a multiple one-phonon phenomenon where magnetisation relaxation occurs by a sequential absorption of phonons involving excited m_J states and then sequential emission of phonons to reach the ground state by reversing its magnetisation.[1–5,48–50] This Orbach relaxation becomes very slow at low temperatures due to the lack of thermally available phonons to initiate this process.[1,2,4,5,51] The Raman process is similar to the Orbach process, but it involves a virtual intermediate state of lattice and spin system which destroys the blocking barrier of magnetisation reversal (see Fig. 1a for the general description described here).

The three key features that are commonly employed to block the magnetisation relaxation of an SMM are (i) a large m_J ground state ($m_J = \pm J$), (ii) designing a ligand environment around the metal centre to maintain a large separation between successive m_J levels of the bistable ground state and (iii) minimal admixing between the m_J states.[1–4,52] It is worthwhile to mention that the search for potential SIMs fulfilling the criteria (i), (ii), and (iii) is considered within the framework of the Orbach process. In this regard, the recent discovery of dysprosocenium SIMs has divulged the importance of spin–vibration coupling in controlling magnetisation relaxation.[5,46,47,53–58] Although synthetic chemists have extensively tried to control spin–vibration coupling through molecular design, design principles to control such effects are still elusive.[47] Therefore, to design high-performance SIMs, one needs to deepen the understanding of spin–vibrational coupling by theoretical methods.

A recent theoretical study also demonstrated that further enhancement of T_B and U_{eff} is challenging in dysprosium complexes as magnetic anisotropy reaches its axial limit.[5] In this regard, the pentagonal bipyramidal family of SIMs has an edge due to a large variation in the U_{eff} (37–1200 cm^{-1}) and T_B (2–30 K) values observed, offering significant room for further improvement in T_B values.[10,11,35,36,38–40,42,59–71] It is noteworthy to mention that raising the T_B value from 60 K to 80 K in dysprosocenium complexes is related to the judicial design of ligands to efficiently decouple the vibrationally active normal mode coupled to the spin states.[46] To fine-tune the magnetic anisotropy in pentagonal bipyramidal Dy(III) SIMs, one needs a thorough understanding of the related spin–phonon coupling. Spin–vibration coupling occurs when a molecular vibration (due to the temperature) modulates the crystal field Hamiltonian of a metal centre. This coupling is directly related to spin–lattice relaxation, and over the past few years, an in-depth investigation of spin–vibration coupling by *ab initio* CASSCF methods has been reported. However, such studies are limited only to a handful of molecules as these calculations are computationally demanding, and alternative methods that are still accurate in understanding the spin–phonon/vibrational problem are of supreme interest to the community.[1–5,38,46,71,72] Although efforts have been made to employ semiempirical methods, they lack the predictive potential for such systems.[8,9,72]

In this work, employing a combination of DFT and the *ab initio* SA-CASSCF/RASSI-SO/SINGLE_ANISO approach, we have studied in detail the pentagonal bipyramidal family of molecules to thoroughly understand their electronic structure and spin–vibrational correlations to the blocking temperatures. The approach established in this work leverages the Boltzmann distribution and oscillator strength of vibrational modes, eliminating the necessity for conducting numerous CASSCF calculations to extract pertinent chemical insights. For our study, we have chosen five pseudo pentagonal bipyramidal Dy(III) SIMs, namely [Dy(bbpen)Br] (**1**, H_2bbpen = *N*,*N*′-bis(2-hydroxybenzyl)-*N*,*N*′-bis(2-methylpyridyl)ethylenediamine),[38] $[Dy(OCMe_3)Br(THF)_5][BPh_4]$ (**2**)[43] and $[Dy(OSiMe_3)Br(THF)_5]$

$[BPh_4]$ (**3**),[43], $[Dy(L^{N5})(Ph_3SiO)_2](BPh_4)\cdot CH_2Cl_2$ (**4**)[73] and $[L_2Dy(H_2O)_5][I]_3\cdot L_2\cdot H_2O$ (**5**, L = ^{t}BuPO(NH^{i}Pr)$_2$)[35] where the U_{eff} and T_B (from FC/ZFC) range from 400–1200 cm^{-1} and 9–16 K, respectively (see Fig. 1b–f and Table S1‡). For the dysprosocenium class of molecules, T_B values are approximately similar, but a pentagonal bipyramidal family of complexes has more diverse U_{eff} and T_B values (see Table S1‡), suggesting room for further enhancement. Here, by performing the spin–vibration calculations, we aim to address the following: (i) Why do the pentagonal bipyramidal Dy(III) SIMs, despite possessing similar structures and U_{eff} values, have a diverse set of T_B values (4.5 K – 36 K, see Table S1‡)? (ii) What is the nature of vibrationally active normal mode causing the transition from the ground KD (Kramers Doublet) to the first excited KD in this class of compounds? (iii) How are these spin–phonon vibrations correlated with the T_B values? (iv) Is it possible to quench vibrations that cause relaxation *via* judicial choice of ligand design? (v) What are the design clues that need to be factored in to enhance the T_B values in this class of molecule?

1.1 Computational procedures for spin–phonon relaxation

The vibrational modes of a complex were determined from the geometry optimisation in the gas phase within the DFT framework (see computational details). Frequency calculations were utilised to confirm that the optimised geometries are true minima on the potential energy surface.[46,53]

In the absence of a magnetic field, the effective Hamiltonian can be written as;[74]

$$\hat{H}_{eff} = \hat{H}_s \otimes \mathbb{I}_{vib} + \mathbb{I}_s \otimes \hat{H}_{vib} + \hat{H}_{s-vib} \quad (1)$$

where H_s, H_{vib} and H_{s-vib} represent the crystal field (spin-system), vibration and spin–vibrational Hamiltonian.

$$\hat{H}_s = \hat{H}_{CF} = \sum_{k=2,4,6}\sum_{q=-k}^{k} B_k^q \tilde{O}_k^q \quad (2)$$

$$\hat{H}_{vib} = \sum_j \hbar\omega_j (n_j + 1/2) \quad (3)$$

$$\hat{H}_{s-vib} = \sum_j \hat{Q}_j \left(\frac{\partial B_k^q}{\partial Q_j}\right)_0 \tilde{O}_k^q(J) \quad (4)$$

Here, B_k^q and $\tilde{O}_k^q(J)$ represent the CF parameters and Stevens operator, respectively. The k, referred to as ranks, runs to $2J$. The components of q range from $-k$ to $+k$ for each k. The total angular momentum defined in the M_J basis ranges from $-M_J$ to $+M_J$ (for Dy^{3+}, $J = \frac{15}{2}$ and M_J runs over $\{-\frac{15}{2}, -\frac{13}{2}, \ldots, +\frac{15}{2}, +\frac{13}{2}\}$). The ω_j and n_j correspond to the

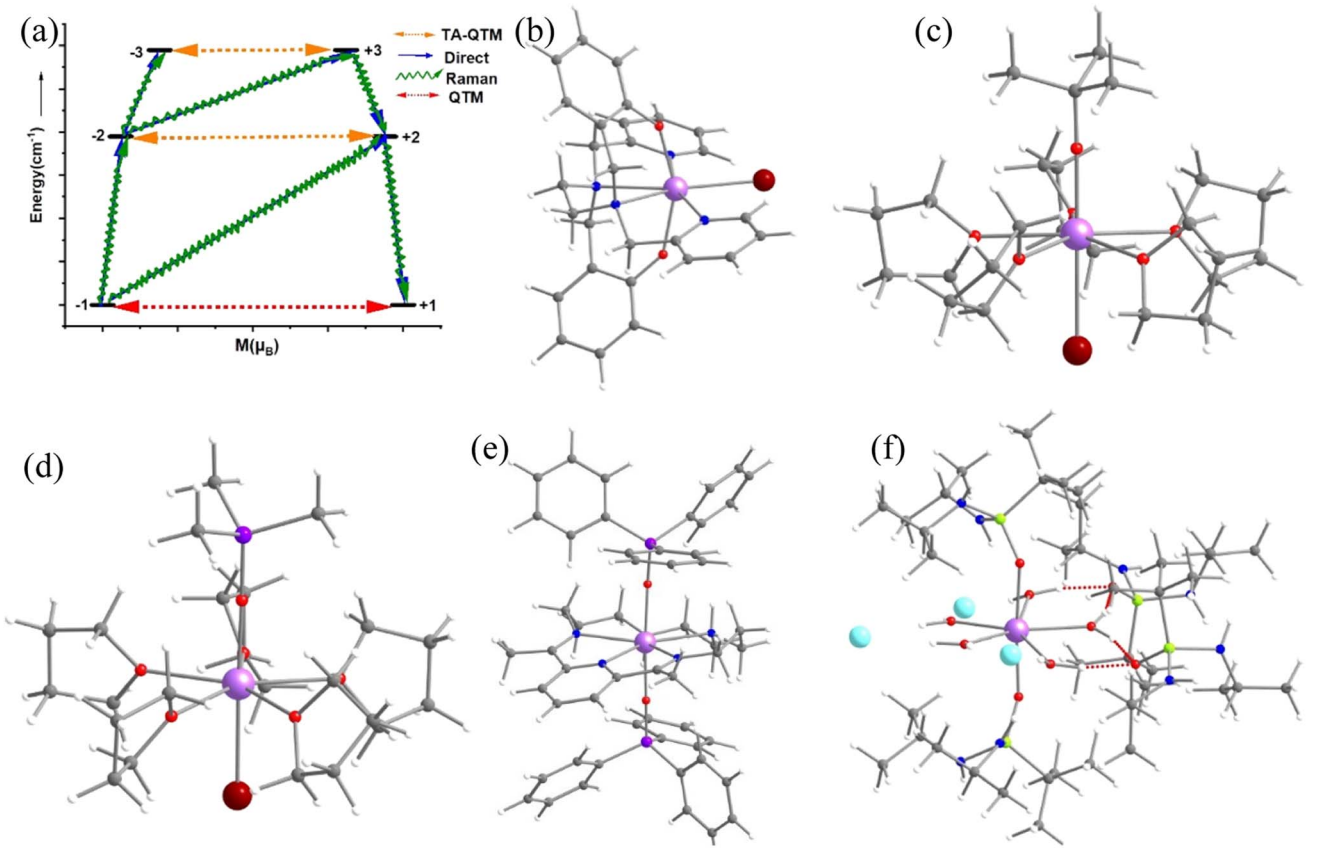

Fig. 1 (a) The general magnetisation relaxation diagram. Here, red arrows denote the QTM for the ground state and TA-QTM (orange) for the excited state. The blue arrows signify the direct/Orbach process. The green arrow implies the Raman process. The crystal structure of complexes (b) [Dy(bbpen)Br] **1**, (c) $[Dy(OCMe_3)Br(THF)_5][BPh_4]$ **2**, (d) $[Dy(OSiMe_3)Br(THF)_5][BPh_4]$ **3**, (e) $[Dy(L^{N5})(Ph_3SiO)_2](BPh_4)\cdot CH_2Cl_2$ **4** and (f) $[L_2Dy(H_2O)_5][I]_3\cdot L_2H_2O$ **5**. The hydrogens are omitted for clarity. Colour code: Dy-violet, I-cyan Br-brown, O-red, Si-purple, N-blue, and C-grey.

frequency of the vibrational level of mode j. The Q_j^- and $\left(\frac{\partial B_k^q}{\partial Q_j}\right)_0$ represent the vibrational coordinate and vibronic coupling of mode j.

The H_s and H_{vib} in eqn (1) are defined on the basis of $|M_J, n_j\rangle$ using the Kronecker product. Therefore, to define H_{s-vib} on the same basis, we considered a weak coupling regime where vibrations remain unaffected by electronic levels. As a result, the H_{s-vib} can be written as,

$$\left\langle M_j', n_j \pm 1 \middle| \hat{H}_{s-vib} \middle| M_j, n_j \right\rangle = \left\langle M_j', n_j \pm 1 \middle| \sum_{k=2,4,6} \sum_{q=-k}^{k} \hat{Q}_j \left(\frac{\partial B_k^q}{\partial Q_j}\right)_0 \tilde{O}_k{}^q(J) \middle| M_j, n_j \right\rangle = \left\langle M_j' \middle| \sum_{k=2,4,6} \sum_{q=-k}^{k} \left(\frac{\partial B_k^q}{\partial Q_j}\right)_0 \tilde{O}_k{}^q(J) \middle| M_j \right\rangle \times \left\langle n_j \pm 1 \middle| \hat{Q}_j \middle| n_j \right\rangle \quad (5)$$

Here, the first term on the right-hand side represents the electronic coupling and the second term represents the vibrational excitation. To estimate the electronic coupling, we have computed the zero-point energy displacements ($Q_{j,0} = \sqrt{\frac{\hbar\omega_j}{k_j}}$ where ω_j and k_j denote the frequency and force constant of vibrational mode j). The equilibrium geometry was then distorted within the range of $-Q_{j,0} \rightarrow +Q_{j,0}$ along the displacement vectors ($\vec{v}$) for each mode using:

$$\vec{Q}_{dist,j} = \vec{Q}_{eq} + \vec{Q}_{j,0}\vec{v} \quad (6)$$

Then we performed CASSCF/RASSI-SO/SINGLE_ANISO calculations for each distorted geometry ($\vec{Q}_{dist,j}$) and extracted the crystal field parameters (CFPs) in Stevens notation. The extracted CFPs were then fitted using second-order polynomials to obtain the first-order vibronic couplings $\left(\frac{\partial B_k^q}{\partial Q_j}\right)_0$. The overall vibronic coupling strength (S_j) of a given mode is extracted by adding the effect of 27 CFPs as follows:

$$S_j = \sqrt{\frac{1}{3}\sum_k \frac{1}{2k+1} \sum_{q=-k}^{+k} \left| \left(\frac{\partial B_k^q}{\partial Q_j}\right)_0 \right|^2} \quad (7)$$

All the energies of the vibrational modes are calculated using the ($(1 + 1/2)\hbar\omega$) formula, after scaling the frequencies considering the employed computational setup.[75] The methodology developed in this study relies on the Boltzmann distribution and oscillator strength of vibrational modes. It involves the inclusion of all vibrational modes until the sum of Boltzmann populations reaches 1 at 100 K. Among these modes, only those with significant oscillator strength were considered. This approach eliminates the need to perform hundreds of CASSCF calculations, streamlining the process of extracting the relevant chemical insights. For complexes **2–5**, we have only calculated the coupling strength S_j for the vibrational modes having large oscillator strength that has reduced the computational cost significantly.

2. Results and discussion

2.1 Controlling U_{eff} and T_B in complex 1 by intuitive chemical substitution using spin–phonon lens

Complex **1** (see Fig. 1a) is reported to exhibit zero-field slow relaxation of magnetisation with a U_{eff} and T_B value of 712 cm^{-1} and 14 K (sweep rate 20 Oe s^{-1}), respectively.[38] Earlier *ab initio* CASSCF calculations on this complex revealed magnetisation relaxation *via* the third excited KD, yielding a U_{cal} value of 721 cm^{-1} (Fig. 2a), which agrees well with the U_{eff} value. To assess and analyse the role of dynamic correlation, we have also performed CASPT2 calculations (see computational details) for this complex. This yields a U_{cal} value of 701.2 cm^{-1}, which is similar to the CASSCF results. Also, all other metrics related to the magnetic properties are similar for both sets, offering confidence in this methodology (see Table S3‡). The geometry optimisation of **1** yields a geometry closely resembling the X-ray structure (Table S2, Fig. S1 and Appendix S1‡). This is also reflected in the *ab initio* CASSCF calculations, where both X-ray and optimised geometries yield a similar energy spectrum, g-tensors and CF parameters (Tables S3 and S4‡), supporting the methodology used in obtaining good geometries for estimating magnetic properties.

For the spin–phonon coupling calculations, we have selected 35 vibrational modes that possess a total population of 1.00 below 100 K (most of the SMMs show opening of hysteresis below 100 K) assuming Boltzmann distribution (see Fig. 2b, S2–S13 and Table S5‡). The coupling strengths S_j of the 35 vibrational modes of **1** are depicted in Fig. 2c (Table S5 and Fig. S14‡), which implies that the ω_{16} and ω_{26} (Fig. 2c) vibrational modes are associated with a large coupling strength and, therefore, should cause the magnetisation relaxation. Further analysis suggests that these modes are associated with a large oscillator strength, as this leads to a larger degree of deformation of the first and second coordination spheres as witnessed in earlier cases.[46,53,57,74,76] Therefore, we have only considered the vibrational modes with large oscillator strength for complexes **2–5** to reduce the computational cost of spin–phonon coupling. The first excited state of ω_{26} vibrational mode ($\Delta E = 387$ cm^{-1} (KD1–KD2) *vs.* $\upsilon = 397$ cm^{-1} ($(1 + 1/2)\hbar\omega$); the ΔE and υ refer to the Kramers doublet gap and the scaled vibrational frequencies, respectively) is also closer to the KD1–KD2 energy gap which further reinforces that this mode should cause the magnetisation relaxation. The ω_{26} vibrational mode of **1**, which is suggestive of being responsible for magnetisation relaxation, has several functional group movements (Fig. 2). The significant vibrational movement was noted for (i) the hydrogen atom at the meta position of the pyridine rings, (ii) the para position of the phenolate rings, and (iii) the $-CH_2$ linker groups attached to pyridine and phenolate donor atoms (Fig. 2). As these were the key vibrations correlated with magnetisation relaxation, any attempt to quench these vibrations is expected to enhance the effective energy barrier/T_B values. The substitution of these

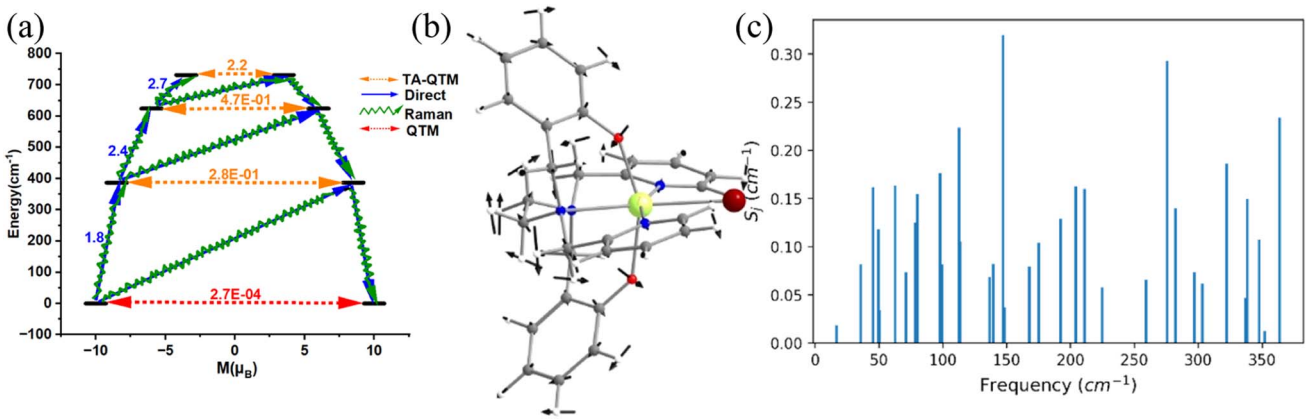

Fig. 2 (a) The mechanism of magnetization relaxation of optimised geometry of **1**. (b) The molecular vibration of **1** corresponds to the ω_{26} frequency (cm^{-1}). Here, the arrows represent the scaled vector of displacement. Colour code: Dy-yellow, Br-brown, O-red, N-blue, C-grey and H-white. (c) The spin–vibrational coupling strength of the first 35 vibrational modes of **1**.

hydrogens will make the vibrational mode off-resonant and is, therefore, expected to improve the performance.

A quick Cambridge structural database search for such substituted geometries reveals substitution of the meta position hydrogen atom by fluorides reported by Li and co-workers [(Dy(bbpen-F)Br], see Fig. 3).[39] We then performed *ab initio* calculations on the optimised geometry (called **1-F**, Appendix S2‡) that yields a U_{cal} value of 763.2 cm^{-1}, which is *ca.* 50 cm^{-1} higher, suggesting enhancement in the effective energy barrier *via* this substitution as expected (Table S6‡). This value matches the experimentally reported U_{eff} value of 798.4 cm^{-1}. More importantly, as expected, the pyridinic contribution to the ω_{26} vibrational mode diminished (Table S7‡), and these are accompanied by a substantial enhancement in the T_B values (14 K@20 Oe s^{-1} to 30 K@20 Oe s^{-1}). This is also corroborated by the decrease in the equatorial ligand field due to the negative inductive ($-I$) effect of the fluoride atom in the equatorial pyridine ring. A similar CCDC search also yielded another structure where the para position of the phenolate hydrogen was substituted by CH_3 groups ([Dy(bbpen-CH_3)Br], **1-pCH$_3$**, see Fig. 3). The *ab initio* calculations on the optimised geometry of **1-pCH$_3$** (Appendix S3‡) yield a U_{cal} value of 764.1 cm^{-1} (Table S8‡), reaffirming a larger value compared to **1** due to an increase in the axial ligand field. Not only does this value match the experimentally reported value of 806.9 cm^{-1}, but the T_B values are also marginally larger (15 K@20 Oe s^{-1}). Furthermore, as expected, the phenolate contribution to the ω_{26} frequencies diminished, leading to a red shift (Table S7‡) of these frequencies in **1-pCH$_3$**. Furthermore, an enhancement of the computed B_2^0 axial CF parameter is observed in **1-F** and **1-pCH$_3$** compared to **1** (Table S3‡).

A further search yielded another structure where the para position of the phenolate hydrogen was substituted by CH_3 groups and para position hydrogen atoms by fluorides ([Dy(bmbpen-F)Br], **1-pCH$_3$F**, see Fig. 3).[77] The *ab initio* calculations on the optimised geometry of **1-pCH$_3$F** (Appendix S4‡) yielded a U_{cal} value of 842.5 cm^{-1}, reaffirming a larger value compared to **1**, **1-F** and **1-pCH$_3$** (Table S9‡). Although the U_{cal} value is slightly overestimated compared to the U_{eff} value of 782.3 cm^{-1}, more importantly, the T_B value (36 K@20 Oe s^{-1}) is

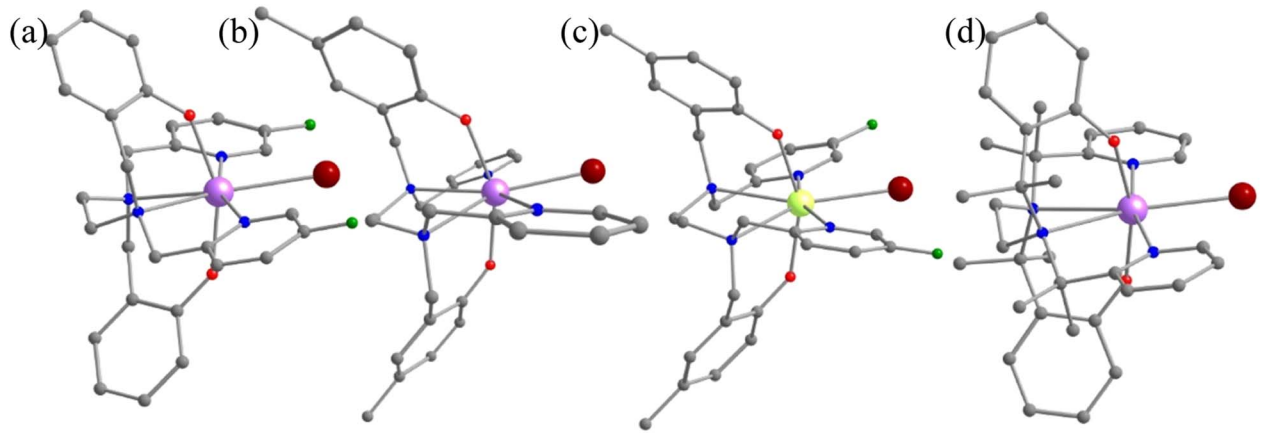

Fig. 3 The crystal structures of (a) **1-F**, (b) **1-pCH$_3$** and (c) **1-pCH$_3$F**. (d) The optimised geometry of **1-CH$_3$**. Here, the hydrogens are omitted for clarity. Colour code: Dy-blue violet, Br-brown, F-green, O-red, N-blue, C-grey.

significantly higher than that of all **1**, **1-F** and **1-pCH$_3$**. As expected, the phenolate and pyridine contributions to the ω_{26} frequencies diminished, leading to a red shift (Table S7‡) of these frequencies in **1-pCH$_3$F**. This reiterates that the approach developed here not only hints at ligand design that targets enhancement in U_{eff} values but also the vibrations that are strongly correlated with the T_B values.

Furthermore, the –CH$_2$ linker groups attached to pyridine and phenolate donors were found to have a significant vibrational movement. We attempted to alter those C–H bonds and modelled the corresponding –CH$_2$ groups using –C(Me)$_2$ groups (see Fig. 3 model **1-CH$_3$**). For this model, the O–Dy–O angle increases to 162.9° and the Dy–N bond length elongates to 2.948 Å (Table S2, Fig. 3 and Appendix S4‡). The *ab initio* CASSCF calculations on **1-CH$_3$** reveal an increase in the KD1–KD2 energy gap, energy splitting of the eight KDs and axial B_2^0 CF parameter compared to **1** by 0.14, 0.50 and 0.06%, respectively (Tables S4 and S10‡). The magnetisation relaxation in **1-CH$_3$** was found to occur *via* the third excited KD, resulting in a U_{cal} value of 1039.5 cm^{-1}, which is *ca.* 300 cm^{-1} larger than that of **1**. Quite interestingly, a red shift of vibrational mode is observed from **1** to **1-CH$_3$** (192.8 cm^{-1} (Table S7‡)). The blocking barrier and normal models of **1**, **1-F**, **1-pCH$_3$**, **1-pCH$_3$F** and **1-CH$_3$** imply that there is a strong correlation between the ω_{26} normal mode and the T_B values.

2.2 Role of the equatorial ligand field in dictating U_{eff} and T_B in complexes 2 and 3

The magnetic properties of complexes **2** and **3** (Fig. 4 and 5) were studied by Zheng and co-workers, along with a family of other pentagonal bipyramidal SMMs. Both of them show zero-field slow relaxation of magnetisation with U_{eff} values of 569 ± 126 (**2**) and 509 ± 49 cm^{-1} (**3**), respectively, with a T_H (blocking temperature derived from the hysteresis loop, see for example ref. 43) value of 9 K (sweep rate 15 Oe s^{-1}).[43] These two complexes are structurally similar, except that the –OCMe$_3$ group present in **2** is replaced by the –OSiMe$_3$ group in **3** (Fig. 4 and 5).[43] This replacement leads to a 0.07 Å enhancement in the Dy–OSiMe$_3$ bond length in **3** compared to Dy–OCMe$_3$ bond length in **2**, resulting in a lower U_{eff} in **3** compared to **2** (Tables S11–S14‡). The geometry optimisation of **2** and **3** also yields geometries and magnetic properties similar to those of X-ray structures (Table S11, Fig. S16, and Appendix S5 and S6‡), and particularly the estimated CF parameters are strikingly similar (see Table S15‡). The *ab initio* CASSCF (CASPT2) calculations performed on these complexes yield a U_{cal} value of 492.9 cm^{-1} (488.8 cm^{-1}) and 570.2 cm^{-1} (553.8 cm^{-1}) for **2** and **3**, respectively. These values are in agreement with experiments and further iterate that dynamic correlations incorporated *via* the CASPT2 method have not substantially modified the metric of magnetic properties estimated, and therefore, it is safe to proceed further with the CASSCF calculations (see Tables S13 and S14‡).

To find out the most important vibrational modes for spin–phonon coupling, we have selected 21 vibrational modes (Fig. 4, S17–S23 and Table S16‡) for **2** and 13 vibrational modes with the energy for **3** (Fig. 5, S25–S29, Tables S16 and S17‡). By analysing the coupling strength, we found that ω_7 and ω_8 vibrational modes for **2** and ω_1, ω_{11} and ω_{12} vibrational modes for **3** are responsible for the spin–phonon coupling from the KD1 to the KD2 transition (Fig. 4, 5, S23, S30 and Tables S16 and S17‡). The second excited state of ω_7 vibrational mode of **2** and ω_1 vibrational mode of **3** (ΔE = 361 cm^{-1} *vs.* υ = 390 cm^{-1}) for **2** and 360 cm^{-1} (ΔE) *vs.* 370 cm^{-1} (υ) for **3** is also closer to the KD1–KD2 energy gap, which further reinforces that these modes should cause magnetisation relaxation. These vibrational modes have a significant impact on many functional groups. Among these vibrations, the displacement of the Dy ion was found to be prominent (Fig. 4 and 5). As these vibrations are responsible for magnetisation relaxation, any attempt to quench these vibrations will increase the U_{eff}/T_B values. Therefore, to quench the in-plane movement of the Dy atom, there are two approaches: (i) substituting the Dy with a heavier isotopic analogue[78–80] and (ii) enhancing the Dy–ligand equatorial bond strength. To achieve this, we have replaced the five THF molecules in the equatorial plane in complexes **2** and **3** with a 16-

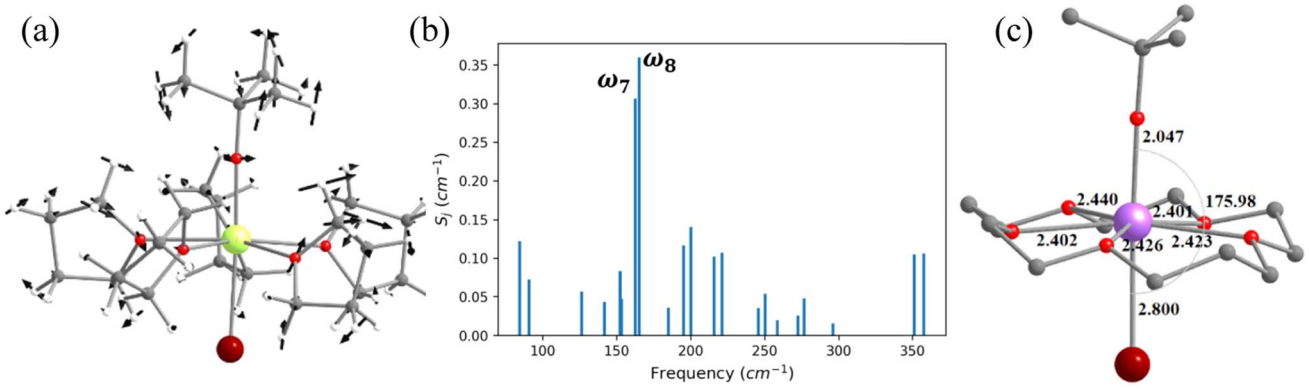

Fig. 4 (a) The molecular vibration of **2** corresponds to ω_8 cm^{-1}. Here, the arrows represent the scaled vector of displacement. Colour code: Dy-yellow, Br-brown, Si-purple, O-red, C-grey and H-white. (b) The coupling strength for the twenty-one high-intensity vibrational modes of **2**. (c) B3LYP optimised model structures of **2-crown**, with important structural parameters (bond lengths are shown in Å and bond angles are shown in °).

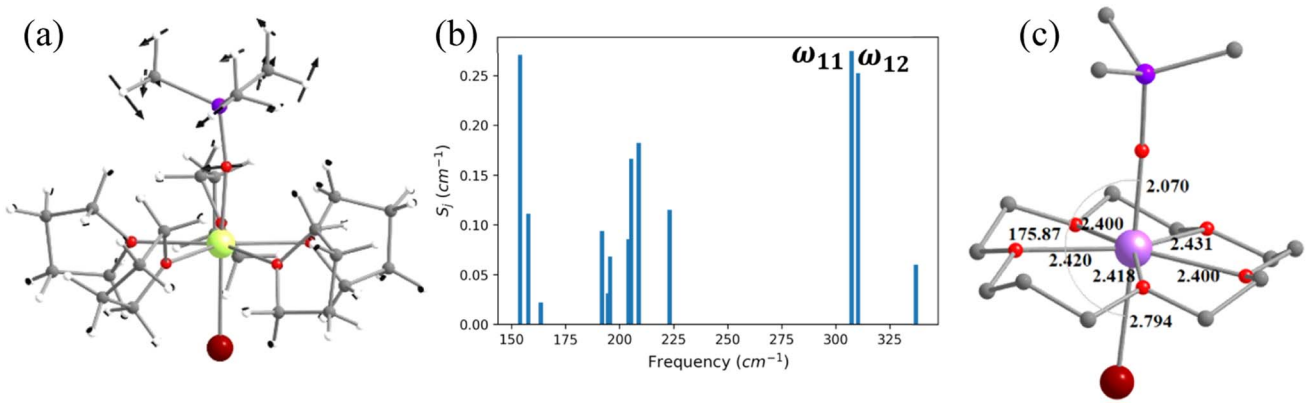

Fig. 5 (a) The molecular vibration of **3** corresponds to ω_{11} cm^{-1}. Here, the arrows represent the scaled vector of displacement. Colour code: Dy-yellow, Br-brown, Si-purple, O-red, C-grey and H-white. (b) The coupling strength for the thirteen high intensity vibrational modes of **3**. (c) B3LYP optimised model structures of **3-crown** with important structural parameters (bond lengths are shown in Å and bond angles are shown in °).

crown-5 macrocyclic ring (models **2-crown** and **3-crown**, see Fig. 3(d) and 4(d)). Although these are models at present, some of us have recently reported [{(18-crown-6)Ln(dippH)$_3$}{(18-crown-6)Ln(dippH)$_2$(dippH$_2$)}]·[I$_3$] (with Ln = Ce, Pr and Nd and dippH$_2$ = 2,6-diisopropylphenylphosphates) complexes of a similar kind with various lanthanide ions exhibiting attractive SIM characteristics.[81–83] The **2-crown** and **3-crown** have shorter Dy–O bond lengths (reduced by ∼0.02–0.04 Å, except Dy–Br bond length) and a marginal 1–2° increase in the O–Dy–Br angle compared to **2** and **3** (Fig. 4c, 5(c), Tables S11 and S12, and Appendix S7 and S8‡).

The *ab initio* calculations reveal enhancement of the KD1–KD2 energy gap, the energy splitting of the eight KDs, as well as axial B_2^0 CF parameters in **2-crown** (**3-crown**) compared to **2** (**3**) (Tables S15, S18 and S19‡). The magnetisation relaxation of **2-crown** (**3-crown**) is expected to take place *via* the 3rd excited KD due to the large thermally assisted quantum tunnelling of magnetisation (TA-QTM)value, yielding a U_{cal} value of 832.8 cm^{-1} (869.1) cm^{-1}, *ca.* 300 (350) cm^{-1} larger than that of **2** (**3**). It is worthwhile to mention that the contribution of the in-plane movement of the Dy atom to the ω_7 (ω_1 for **3-crown**) frequencies diminished, leading to a red shift (Table S20‡) of these frequencies, and this is expected to enhance the T_B values.

2.3 Role of N–H vibrations in fine-tuning the U_{eff} and T_B values in complex 4

In the earlier section, we have shown how a crown-ether ligand in the equatorial position quenches the low-energy vibrational modes that are correlated with the magnetisation relaxation. These two models are predictions, but an analogous complex containing a macrocyclic Schiff-based ligand at the equatorial position has been reported earlier by Murrie and our group [Dy(L^{N5})(Ph$_3$SiO)$_2$](BPh$_4$)·CH$_2$Cl$_2$ (**4**, Fig. 6).[73] However, due to the complexity of the functional groups involved in the equatorial position, similar vibrations in **4** were absent. We have carefully analysed various vibrational modes at the equatorial plane, which could help improve the performance of **4**. Complex **4** exhibits zero-field slow relaxation of magnetisation with a very large U_{eff} of 791.4 cm^{-1} and T_B of 14 K (sweep rate 100 Oe s^{-1}). The *ab initio* calculations on this complex yield a U_{cal} value that is in excellent agreement with the U_{eff} value reported (791.4 *vs.* 722.8 cm^{-1}). On the other hand, the O–Dy–O angle reduces to 2.5° in the optimised structure compared to the X-ray geometry (Tables S21, S22 and Fig. S31‡), and the optimised geometry yields magnetic characteristics and CF parameters, which are similar to those of the X-ray structure (see Tables S22 and S23‡).

For the spin–phonon coupling calculations of **4**, we selected nineteen vibrational modes (Fig. S32–S38 and Table S24‡) with a large oscillator strength in the range of KD1–KD2 energy gap. By analysing the coupling strength (Fig. 6, S39 and Table S24‡), we found that the ω_{17} and ω_{18} vibrational modes are likely to be responsible for the spin–phonon coupling of the KD1 → KD2 transition. These vibrations are found to be correlated with the N–H vibrations present in the equatorial plane (Fig. 6). To quench these vibrations, we have replaced the –NH group with its isoelectronic analogue oxygens resulting in **4-N$_3$O$_2$** (Fig. 6 and Appendix S10‡). As expected, a red shift of the ω_{17} vibrational mode (327.1 (**4**) cm^{-1} → 377.2 cm^{-1} (**4-N$_3$O$_2$**) cm^{-1}, Table S26‡) is observed in **4-N$_3$O$_2$**. The *ab initio* calculations on **4-N$_3$O$_2$** revealed an enhancement in the energy splitting of the eight KDs compared to **4** (Table S25‡). The magnetisation relaxation of **4-N$_3$O$_2$** occurs *via* the third excited KD due to significant transverse anisotropy yielding a U_{cal} value of 998.7 cm^{-1} (Table S25‡), which is *ca.* 200 cm^{-1} larger than that of **4**.

2.4 Role of out-of-plane bending of water in controlling the U_{eff} and T_B values in complex 5

In this last section, we will unveil the nature of vibration correlated with the magnetisation relaxation in the [L$_2$Dy(H$_2$O)$_5$]$^{3+}$ family of SMMs where a large U_{eff} and T_B were observed (Fig. 7).[35,36,60,61,67,84] The complex **5** is reported to possess a large U_{eff} value and T_B value of 453 cm^{-1} and 16 K (sweep rate 20 Oe s^{-1}), respectively.[35] The *ab initio* CASSCF calculations on the X-ray structure of **5** indicated that the

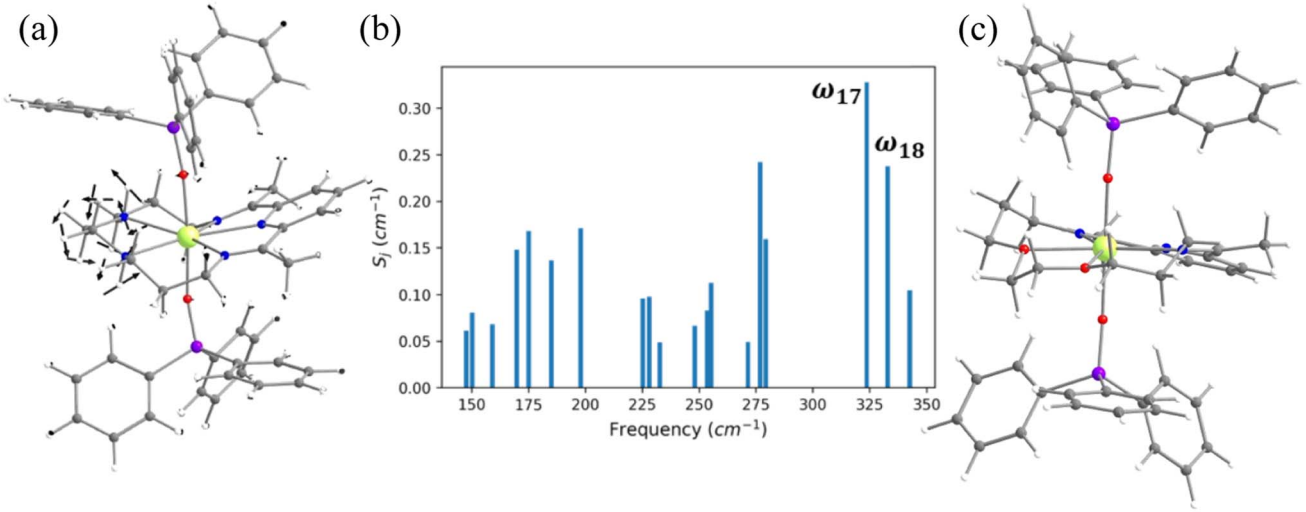

Fig. 6 (a) The molecular vibration of **4** corresponding to the ω_{17} vibrational mode. Here, the arrows represent the scaled vector of displacement. Colour code: Dy-yellow, Si-purple, O-red, N-blue, C-grey and H-white. (b) The coupling strength for the nineteen high IR intensity vibrational modes of **4**. (c)The optimised geometry of **4-N_3O_2**.

stabilisation of $m_J = |\pm 15/2\rangle$ and $|\pm 13/2\rangle$ in the ground and first excited state, respectively. The magnetisation relaxation occurs *via* the second excited KD, yielding a U_{cal} value of 471.3 cm^{-1}, slightly overestimated compared to the U_{eff} value (Table S27‡). The *ab initio* calculations on this optimised structure reveal a moderate change in energy values and g tensors compared to the X-ray geometry as the equatorial oxygens become out-of-plane in the optimised structure (Table S28, Fig. S40 and Appendix S11‡). However, the computed CF parameters in the optimised structure are similar (Table S29‡) to those in the X-ray structure, and more importantly, the ground and first excited KDs possess dominant contributions from $m_J = |\pm 15/2\rangle$ and $|\pm 13/2\rangle$ states, respectively.

For the spin–phonon coupling calculations on **5**, we selected twenty-seven vibrational modes (shown in Fig. 7, S41–S49 and Table S30‡). The CF parameter values at the several displacements of these normal modes are shown in Fig. S50.‡ By analysing the coupling strength, we find that the ω_8 and ω_{14} vibrational modes are likely responsible for the spin–phonon coupling of the KD1 → KD2 transition. The second excited state of ω_8 vibrational mode of **2** ($\Delta E = 268$ cm^{-1} *vs.* $\upsilon = 282$ cm^{-1}) is also closer to the KD1–KD2 energy gap, which further reinforces that these modes should cause the magnetisation relaxation. These ω_8 and ω_{14} and ω_{13}, vibrational modes have a significant movement for the equatorial oxygens (out-of-plane) and axial –CH_3 groups. Therefore, quenching the movement of the equatorial oxygens should increase the U_{eff} and T_B values of **5**.

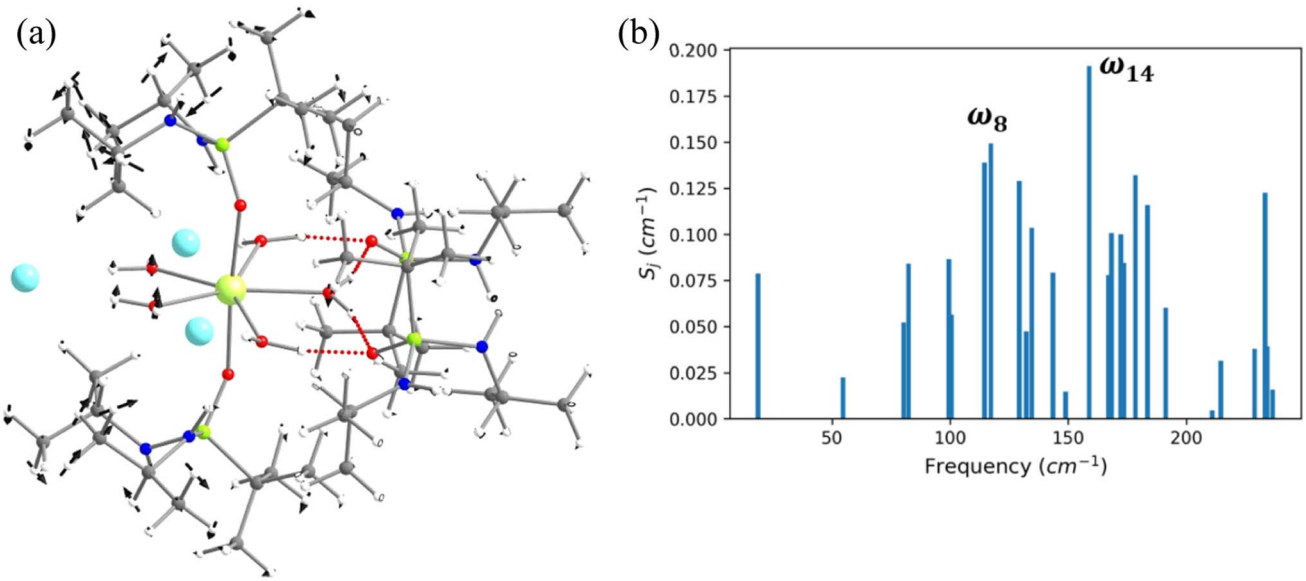

Fig. 7 (a) The molecular vibration of **5** corresponds to the ω_8 vibrational mode. Here, the arrows represent the scaled vector of displacement. (b) The spin–vibrational coupling strength for the twenty seven high IR intensity vibrational modes of **5**.

3. Discussion

The advancement in molecular nanomagnets has led to the growth of plenty of SMMs with very large U_{eff} values, but the T_B values remain a small fraction of them due to the under-barrier relaxation processes. In this regard, the study of spin–phonon coupling in dysprosocenium complex $[Dy(Cp^{ttt})_2][B(C_6F_5)_4]$ ($Cp^{ttt} = \{C_5H_2{}^tBu_3\text{-}1,2,4\}$) has made an important breakthrough, not only because this holds a record high T_B value, but also because they have shown which vibrations are linked with the magnetisation relaxation.[46] Based on their study, two years later, another novel dysprosocenium SIM, $[(Cp^{iPr5})Dy(Cp^*)]^+$ (Cp^{iPr5}, penta-iso-propylcyclopentadienyl; Cp*, pentamethylcyclopentadienyl) was discovered quenching the vibrations governing the magnetisation relaxation.[53] On the other hand, Lunghi and co-workers recently demonstrated the role of anharmonic phonons in dictating the under-barrier magnetisation relaxation.[1–4,49,52,85–87] Therefore, spin–phonon coupling calculations are of utmost importance to unveil the underlying physical process of magnetisation relaxation and provide a clear indication of how the relaxation process is linked with molecular motions. As a result, it can provide the design criteria for potential SMMs with chemical tuning to quench the vibrations associated with Orbach and Raman relaxation processes.

The calculations of spin–phonon coupling require thousands of *ab initio* calculations, which are computationally demanding and often do not directly yield chemical insights to improve the T_B values. Furthermore, we have confined ourselves to the vibrations having significant oscillator strength that also lies within the KD1–KD2 energy gap so that magnetisation relaxation from $m_J = |\pm 15/2\rangle$ to $|\pm 13/2\rangle$ of the ground $^6H_{15/2}$ state can be gauged.[46,57,74,76,88,89] Our calculations reveal that not only the atoms in the first coordination sphere but also those in the secondary coordination sphere affect the magnetisation relaxation. In the case of complex **5**, the out-of-plane bending vibrations of the equatorial oxygens govern the magnetisation relaxation, and therefore, disrupting this movement might increase the U_{eff} and T_B values. It is worth mentioning that in the Cl and Br analogues of complex **5** ($[L_2Dy(H_2O)_5][Cl]_3\cdot L_2$ (**6**) and $[L_2Dy(H_2O)_5][Br]_3\cdot L_2\cdot H_2O$ (**7**), L = ^{t}BuPO(NH^{i}Pr)$_2$), the U_{eff} and T_B values decrease from I to Br and Cl analogues (T_B (sweep rate 20 Oe s^{-1}) = 16.0 K for I, 14.0 K for Br and 9.0 K for Cl).[90] This may be ascribed to the equatorial planarity of water molecules, which decreases from I to Br to Cl analogues of **5**. The vibrational modes should be near-resonant with the KD1–KD2 energy gap for the magnetisation relaxation in the Orbach regime. In our case, the energy of the vibrational modes is far lower than the KD1–KD2 energy gap, diminishing the T_B values. From the literature, we have also found an increase in the T_B value from $[Dy(OPCy_3)(H_2O)_5]Cl_3\cdot OPCy_3\cdot H_2O\cdot EtOH$ (**8**, T_B(sweep rate = 200 Oe s^{-1}) = 11 K) to $[Dy(OPCy_3)(H_2O)_5]Br_3\cdot 2OPCy_3\cdot 2H_2O\cdot 2EtOH$ (**9**, T_B(sweep rate = 200 Oe s^{-1}) = 20 K).[36] On the other hand, a significant improvement in the blocking barrier is observed going from $[Dy(HMPA)_2(H_2O)_5]Cl_3\cdot HMPA$ (**10**, HMPA = U_{eff} = 460 K) to $[Dy(HMPA)_2(H_2O)_5]I_3\cdot 2HMPA$ (**11**, U_{eff} = 600 K).[61] The U_{eff} and T_B values of complexes **8**, **9**, **10** and **11** further support that movement of the oxygen atoms is linked with the magnetisation relaxation in the $[L_2Dy(H_2O)_5]^{3+}$ family of SMMs.

In this manuscript, by analysing the spin–phonon coupling, we have shown that the modulation of geometry *via* simple ligand substitution can shift the vibrations and decouple with the KD1–KD2 gap that is linked with the magnetisation relaxation in **1-F**, **1-pCH$_3$**, **1-pCH$_3$F** and **1-CH$_3$** in comparison with the parent geometry **1**. As a result of this, an enhancement of U_{eff} and T_B values is observed compared to the parent complex. On the other hand, the electrostatic polarisation of the donor atom strongly affects the spin–phonon coupling, as suggested by Lunghi and co-workers.[4] They demonstrated that employing a ligand system where the donor atom charges are not significantly affected by vibrations should lead to a potential SMM. In the case of complexes **2** and **3**, introducing a crown ether ligand in the equatorial position in place of the five THF molecules minimizes the electronic delocalisation, leading to an increase in the U_{eff} values. In the case of complex **4**, the replacement of –NH groups by oxygen also reduces the electronic delocalisation; hence, a significant improvement in the U_{eff} value is observed in **4-N$_3$O$_2$** compared to **4**. It should be noted that the organometallic complex with a haptic ligand and complexes with a carbene ligand show very high T_B values due to the minimal polarisation in the first coordination sphere.

By leveraging the outcomes of spin–phonon calculations conducted on complexes **1–5**, a comprehensive analysis of the T_B values across all studied complexes has become possible, shedding particular light on the intriguingly low values observed in complexes **2** and **3**. It is worthwhile to mention that among complexes **1–5**, the largest T_B value is observed for complex **5** (16 K), followed by **1** ≈ **4** (14 K) and **2** ≈ **3** (9 K). From these values, we can suggest that the T_B value is the lowest for complexes where the significant movement of metals and atoms in the first coordination controls the magnetisation relaxation. This is the case with complexes **2** and **3**, where the vibration involving in-plane movement of the Dy ion is associated with the magnetisation relaxation, and this is primarily due to the flexible first coordination sphere atoms. In the case of complex **4**, the atoms in the second coordination sphere, such as hydrogen atoms of –NH groups, control the magnetisation relaxation. Therefore its T_B is slightly higher than that of complexes **2** and **3**. In the case of complex **1**, the hydrogen atoms associated with the phenyl and pyridine rings in the third coordination sphere govern the magnetisation relaxation. Finally, in the case of complex **5**, the H-bonding interactions with the counter anions are linked with the magnetisation relaxation. As the counter anions involved in this case are beyond the coordination sphere, this complex T_B value is the largest among all. Hence, the establishment of a rigid first coordination sphere surrounding Dy(III) is an imperative requirement when designing prospective SMMs. This should also be accompanied by a minimum electrostatic polarisation of the corresponding donor atoms. Given the diverse nature of associated vibrations within this molecular class, a more extensive dataset encompassing all pentagonal bipyramidal Dy(III) complexes, coupled with the power of AI/ML tools, holds

tremendous potential to forge a path forward. Excitingly, this endeavour is currently underway in our laboratory.

4. Conclusions

In summary, by studying twenty-three molecules/models in the family of pseudo-D_{5h} Dy(III) single-ion magnets using DFT and *ab initio* CASSCF calculations, we have deciphered the large variation in the blocking temperature (T_B) observed in this class of molecules. The variation observed was attributed to the interplay between the spin–vibrational coupling and crystal field splitting of the ground state. The $J = 15/2$ term of the $^6H_{15/2}$ ground state is split into $2J$ m_J crystal field sub-states. We begin with complex **1**, where ω_{26} normal mode vibrations have multiple atom movements that include C–H bond vibrations of (i) the meta position of pyridine rings, (ii) the para position of the phenolate rings, and (iii) the $-CH_2$ linker connecting the amine nitrogen atom with pyridine/phenolate donor atoms. We then discovered molecules from the literature where this vibrational mode was restricted in several analogous molecules **1-F**, **1-pCH$_3$**, **1-pCH$_3$F** and **1-CH$_3$** that systematically attempt to shift the ω_{26} normal mode to create an off-resonance scenario with the relaxation mechanism. The next set contains molecules **2** and **3**, whose flexible first coordination sphere yields inferior SIM performance. To circumvent this problem, **2-crown** and **3-crown** were modelled with a rigid first coordination sphere, yielding better performance. Complex **4** has a macrocyclic Schiff-based ligand at the equatorial position, where N–H vibrations were the weak point and model **4-N$_3$O$_2$** aims to address this issue. Complex **5**, on the other hand, has five water molecules in the equatorial plane, and out-of-plane bending of the water molecules is a major factor in the relaxation mechanism. Although this cannot be eliminated, complexes **6** and **7** with –Cl and –Br analogues are added to affirm this point in this class of molecules. Complexes **8**, **9**, **10** and **11** have a similar ligand framework but with a variation in the secondary coordination sphere and were studied to probe this effect. The main conclusions drawn from our work are mentioned below.

4.1 Predicting and enhancing the T_B by recognising the vibration responsible for relaxation

In the [Dy(bbpen)Br] (**1**) complex and analogue structures with substitution on the ligand periphery (such as **1-F**, **1-pCH$_3$**, **1-pCH$_3$F**), the ω_{26} vibration corresponds to the vibrations of donor atoms at the first coordination sphere. This is due to the flexible coordination sphere provided by the ligand framework. Any chemical substitution that shifts this vibration is expected to enhance the T_B values. Quite interestingly, this coincides with a literature report where such substitution performed by a trial-and-error method was found to improvise the T_B values, affirming faith in the model proposed. Armed with such outcomes, we further targeted the $-CH_2$ linkers that connect the amine nitrogen atom to the pyridinic ring at the equatorial positions and *in silico* models have been proposed to boost the T_B values further.

4.2 Importance of the equatorial ligand field in dictating T_B

The two complexes $[Dy(OCMe_3)Br(THF)_5][BPh_4]$ (**2**) and $[Dy(OSiMe_3)Br(THF)_5][BPh_4]$ (**3**) studied exhibit very low T_B values and these are attributed to the vibration involving the asymmetric stretching of the O–Dy–Br bond along the axial direction coupled with in plane bending of the equatorial THF molecule. This is essentially due to the very weak equatorial coordination that provides enhanced axiality as desired but also offers low in-plane bendings, which causes magnetisation relaxation, reducing the T_B values. To arrest such movements, we have *in silico*-modelled geometries where a crown ether ligand replaced five THF molecules. This model is expected to boost the T_B value further. Studies on $[Dy(L^{N5})(Ph_3SiO)_2](BPh_4)\cdot CH_2Cl_2$ (**4**) reveal a similar scenario, and a suitable ligand substitution (N–H by O) was offered to boost the performance.

4.3 Controlling H-bonding interactions to improve T_B values

Our calculations on $[L_2Dy(H_2O)_5][I]_3\cdot L_2\cdot H_2O$ (**5**) suggest that out-of-plane bending of the water molecules is one of the major factors in the relaxation mechanism. As these water molecules are in H-bonding interaction with the counteranions, efforts to modulate these vibrations will be proven to be beneficial. There are already literature reports where the T_B values were found to be enhanced if the equatorial planarity of the water molecules was improved *via* ligand design/cluster aggregation.

Through the meticulous execution of DFT and *ab initio* CASSCF calculations on a comprehensive set of pentagonal bipyramidal complexes/models, we have successfully elucidated the underlying factors contributing to the significant variation in T_B values within this family. Moreover, we present a chemically viable methodology to fine-tune the performance of this intriguing molecular class for the first time.

5. Methodology

All the gas phase geometry optimisations and calculations of normal modes of complexes **1–5** were performed within the unrestricted DFT framework utilizing the Gaussian09 programme package.[91] The X-ray structure (without counter anions and solvent molecules except in complex **5**) was employed as a starting point for geometry optimisation. The hybrid B3LYP exchange-correlation functional (including dispersion corrections for **5**) was employed for the geometry optimisation.[92–94] The Dy(III) ion was replaced by Y(III) to aid smooth SCF convergence. We have used Stuttgart's effective core potential (SDD ECP, 28 core electrons) basis set for yttrium and iodine atoms.[95,96] For other elements, a 6-31G* basis set was employed.[97] For the geometry optimisation of model complexes, we have used SDD for yttrium and iodine, the Ahlrichs triple-ζ plus polarisation basis set for oxygen, nitrogen, fluorine and bromine and the 6-31G* basis set for carbon and hydrogen atoms.[95–98] We have also optimised structures **1** and **2**, taking Dy as the central ion by employing the triple zeta basis set utilizing Cundari–Stevens (CS) relativistic effective core potential (Fig. S51‡). We have observed that it makes minimal changes with respect to the former structures. Therefore, for the

remainder of the manuscript, we have exclusively used Y. The harmonic vibrational modes and vibrational spectra were estimated with an isotope mass of 162.5 (the mass of the most abundant isotope of dysprosium) for the yttrium atom to obtain the correct reduced masses.[72,76]

All the *ab initio* CASSCF/RASSI-SO/SINGLE_ANISO calculations on the X-ray, optimised, and model complexes were performed using the MOLCAS 8.2 programme package.[99] We have used Douglas–Kroll–Hess (DKH) Hamiltonian to take into account the relativistic effect of the metal centre.[100] The Cholesky decomposition technique was used to reduce the size of the disk space.[101] The basis sets of our calculations have been taken from the ANO-RCC (atomic natural orbital-relativistically core correlated) library available in MOLCAS. Here, we have used the VTZP quality basis set for Dy, the VDZP quality basis set for the atoms in the first coordination sphere, and the VDZ quality basis set for the atoms from the secondary coordination sphere onwards. The active space for the complete active space self-consistent field (CASSCF) calculations consists of nine 4f electrons in seven 4f orbitals of Dy(III). We have performed state average CASSCF calculations for the twenty-one sextets of Dy(III) ions. The quartet and doublet spin states of Dy(III) were not considered in our calculations to reduce the computational cost since they do not contribute significantly to the spin–orbit energies, as seen from earlier studies. However, the twenty-one spin-free states were mixed by spin–orbit coupling in the RASSI-SO module. Thereafter, the SINGLE_ANISO module was used to compute the g-tensors, crystal field parameters, and magnetic properties such as susceptibility, QTM, TA-QTM *etc.* To incorporate dynamic correlations we have also performed complete active space second order perturbation theory (CASPT2) calculations for complexes **1**, **2** and **3**, where the U_{cal} values found were similar to those of CASSCF (complexes **1-caspt2**, **2-caspt2** and **3-caspt2** given in Tables S3, S13 and S14‡).

Data availability

The datasets supporting this article have been uploaded as part of the ESI.‡

Author contributions

GR has designed and executed the project. SD and TS performed all calculations and also contributed to the manuscript writing.

Conflicts of interest

There are no conflicts to declare.

Acknowledgements

We thank IIT Bombay for its supercomputing facility. S. D thanks IIT Bombay for an IPDF fellowship. G. R. would like to acknowledge DST and SERB (CRG/2018/00430; SB/SJF/2019-20/12; and SPR/2019/001145) for funding. TS is thankful to CSIR for the fellowship. We thank Dr Aman Ullah (ICMol, University of Valencia) for providing effective insights during the calculations and analysis.

References

1 A. Lunghi, F. Totti, S. Sanvito and R. Sessoli, *Chem. Sci.*, 2017, **8**, 6051–6059.
2 A. Lunghi, F. Totti, R. Sessoli and S. Sanvito, *Nat. Commun.*, 2017, **8**, 1–7.
3 A. Lunghi and S. Sanvito, *J. Chem. Phys.*, 2020, **153**, 174113.
4 M. Briganti, F. Santanni, L. Tesi, F. Totti, R. Sessoli and A. Lunghi, *J. Am. Chem. Soc.*, 2021, **143**, 13633–13645.
5 D. Reta, J. G. C. Kragskow and N. F. Chilton, *J. Am. Chem. Soc.*, 2021, **143**, 5943–5950.
6 C. A. Gould, K. R. McClain, D. Reta, J. G. Kragskow, D. A. Marchiori, E. Lachman, E.-S. Choi, J. G. Analytis, R. D. Britt and N. F. Chilton, *Science*, 2022, **375**, 198–202.
7 J. G. Kragskow, J. Marbey, C. D. Buch, J. Nehrkorn, M. Ozerov, S. Piligkos, S. Hill and N. F. Chilton, *Nat. Commun.*, 2022, **13**, 1–10.
8 L. Escalera-Moreno, J. J. Baldoví, A. Gaita-Ariño and E. Coronado, *Chem. Sci.*, 2018, **9**, 3265–3275.
9 L. Escalera-Moreno, J. J. Baldoví, A. Gaita-Arino and E. Coronado, *Chem. Sci.*, 2020, **11**, 1593–1598.
10 A. K. Bar, P. Kalita, M. K. Singh, G. Rajaraman and V. Chandrasekhar, *Coord. Chem. Rev.*, 2018, **367**, 163–216.
11 S. G. McAdams, A.-M. Ariciu, A. K. Kostopoulos, J. P. Walsh and F. Tuna, *Coord. Chem. Rev.*, 2017, **346**, 216–239.
12 S. T. Liddle and J. van Slageren, *Chem. Soc. Rev.*, 2015, **44**, 6655–6669.
13 N. Ishikawa, M. Sugita, T. Ishikawa, S.-y. Koshihara and Y. Kaizu, *J. Am. Chem. Soc.*, 2003, **125**, 8694–8695.
14 R. J. Blagg, L. Ungur, F. Tuna, J. Speak, P. Comar, D. Collison, W. Wernsdorfer, E. J. McInnes, L. F. Chibotaru and R. E. Winpenny, *Nat. Chem.*, 2013, **5**, 673–678.
15 R. J. Blagg, C. A. Muryn, E. J. McInnes, F. Tuna and R. E. Winpenny, *Angew. Chem.*, 2011, **123**, 6660–6663.
16 R. J. Blagg, F. Tuna, E. J. McInnes and R. E. Winpenny, *Chem. Commun.*, 2011, **47**, 10587–10589.
17 L. Ungur, J. J. Le Roy, I. Korobkov, M. Murugesu and L. F. Chibotaru, *Angew. Chem.*, 2014, **126**, 4502–4506.
18 S.-D. Jiang, B.-W. Wang, H.-L. Sun, Z.-M. Wang and S. Gao, *J. Am. Chem. Soc.*, 2011, **133**, 4730–4733.
19 J. J. Le Roy, I. Korobkov and M. Murugesu, *Chem. Commun.*, 2014, **50**, 1602–1604.
20 J. J. Le Roy, M. Jeletic, S. I. Gorelsky, I. Korobkov, L. Ungur, L. F. Chibotaru and M. Murugesu, *J. Am. Chem. Soc.*, 2013, **135**, 3502–3510.
21 S. Demir, J. M. Zadrozny and J. R. Long, *Chem.–Eur. J.*, 2014, **20**, 9524–9529.
22 A. J. Brown, D. Pinkowicz, M. R. Saber and K. R. Dunbar, *Angew. Chem.*, 2015, **127**, 5962–5966.
23 P. Zhang, L. Zhang, C. Wang, S. Xue, S.-Y. Lin and J. Tang, *J. Am. Chem. Soc.*, 2014, **136**, 4484–4487.
24 D. Tanaka, T. Inose, H. Tanaka, S. Lee, N. Ishikawa and T. Ogawa, *Chem. Commun.*, 2012, **48**, 7796–7798.

25 L. J. Batchelor, I. Cimatti, R. Guillot, F. Tuna, W. Wernsdorfer, L. Ungur, L. F. Chibotaru, V. E. Campbell and T. Mallah, *Dalton Trans.*, 2014, **43**, 12146–12149.
26 A. K. Mondal, S. Goswami and S. Konar, *Dalton Trans.*, 2015, **44**, 5086–5094.
27 W. Cao, C. Gao, Y.-Q. Zhang, D. Qi, T. Liu, K. Wang, C. Duan, S. Gao and J. Jiang, *Chem. Sci.*, 2015, **6**, 5947–5954.
28 S.-S. Liu, K. Lang, Y.-Q. Zhang, Q. Yang, B.-W. Wang and S. Gao, *Dalton Trans.*, 2016, **45**, 8149–8153.
29 K.-X. Yu, Y.-S. Ding, T. Han, J.-D. Leng and Y.-Z. Zheng, *Inorg. Chem. Front.*, 2016, **3**, 1028–1034.
30 Y.-L. Wang, Y. Ma, X. Yang, J. Tang, P. Cheng, Q.-L. Wang, L.-C. Li and D.-Z. Liao, *Inorg. Chem.*, 2013, **52**, 7380–7386.
31 V. E. Campbell, H. Bolvin, E. Rivière, R. Guillot, W. Wernsdorfer and T. Mallah, *Inorg. Chem.*, 2014, **53**, 2598–2605.
32 S. D. Jiang, B. W. Wang, G. Su, Z. M. Wang and S. Gao, *Angew. Chem.*, 2010, **122**, 7610–7613.
33 G.-J. Chen, C.-Y. Gao, J.-L. Tian, J. Tang, W. Gu, X. Liu, S.-P. Yan, D.-Z. Liao and P. Cheng, *Dalton Trans.*, 2011, **40**, 5579–5583.
34 G. J. Chen, Y. N. Guo, J. L. Tian, J. Tang, W. Gu, X. Liu, S. P. Yan, P. Cheng and D. Z. Liao, *Chem.–Eur. J.*, 2012, **18**, 2484–2487.
35 S. K. Gupta, T. Rajeshkumar, G. Rajaraman and R. Murugavel, *Chem. Sci.*, 2016, **7**, 5181–5191.
36 Y.-C. Chen, J.-L. Liu, L. Ungur, J. Liu, Q.-W. Li, L.-F. Wang, Z.-P. Ni, L. F. Chibotaru, X.-M. Chen and M.-L. Tong, *J. Am. Chem. Soc.*, 2016, **138**, 2829–2837.
37 Y. S. Ding, N. F. Chilton, R. E. Winpenny and Y. Z. Zheng, *Angew. Chem., Int. Ed.*, 2016, **55**, 16071–16074.
38 J. Liu, Y.-C. Chen, J.-L. Liu, V. Vieru, L. Ungur, J.-H. Jia, L. F. Chibotaru, Y. Lan, W. Wernsdorfer and S. Gao, *J. Am. Chem. Soc.*, 2016, **138**, 5441–5450.
39 L. Zhu, B. Yin, P. Ma and D. Li, *Inorg. Chem.*, 2020, **59**, 16117–16121.
40 M. Li, H. Wu, Q. Yang, H. Ke, B. Yin, Q. Shi, W. Wang, Q. Wei, G. Xie and S. Chen, *Chem.–Eur. J.*, 2017, **23**, 17775–17787.
41 S. Zhang, H. Wu, L. Sun, H. Ke, S. Chen, B. Yin, Q. Wei, D. Yang and S. Gao, *J. Mater. Chem. C*, 2017, **5**, 1369–1382.
42 Z. Jiang, L. Sun, Q. Yang, B. Yin, H. Ke, J. Han, Q. Wei, G. Xie and S. Chen, *J. Mater. Chem. C*, 2018, **6**, 4273–4280.
43 Y. S. Ding, T. Han, Y. Q. Zhai, D. Reta, N. F. Chilton, R. E. Winpenny and Y. Z. Zheng, *Chem.–Eur. J.*, 2020, **26**, 5893–5902.
44 L. Tesi, A. Lunghi, M. Atzori, E. Lucaccini, L. Sorace, F. Totti and R. Sessoli, *Dalton Trans.*, 2016, **45**, 16635–16643.
45 M. Atzori, L. Tesi, S. Benci, A. Lunghi, R. Righini, A. Taschin, R. Torre, L. Sorace and R. Sessoli, *J. Am. Chem. Soc.*, 2017, **139**, 4338–4341.
46 C. A. P. Goodwin, F. Ortu, D. Reta, N. F. Chilton and D. P. Mills, *Nature*, 2017, **548**, 439–442.
47 K. R. McClain, C. A. Gould, K. Chakarawet, S. J. Teat, T. J. Groshens, J. R. Long and B. G. Harvey, *Chem. Sci.*, 2018, **9**, 8492–8503.
48 A. Lunghi and S. Sanvito, *Sci. Adv.*, 2019, **5**, eaax7163.
49 A. Lunghi, *Appl. Magn. Reson.*, 2020, **51**, 1343–1356.
50 R. Nabi, J. Kragskow, J. Staab, D. Reta, J. Skelton and N. Chilton, *J. Am. Chem. Soc.*, 2023, **145**, 24558–24567.
51 S. Mondal and A. Lunghi, *J. Am. Chem. Soc.*, 2022, **144**, 22965–22975.
52 A. Albino, S. Benci, L. Tesi, M. Atzori, R. Torre, S. Sanvito, R. Sessoli and A. Lunghi, *Inorg. Chem.*, 2019, **58**, 10260–10268.
53 F.-S. Guo, B. M. Day, Y.-C. Chen, M.-L. Tong, A. Mansikkamäki and R. A. Layfield, *Science*, 2018, **362**, 1400–1403.
54 C. A. Goodwin, D. Reta, F. Ortu, J. Liu, N. F. Chilton and D. P. Mills, *Chem. Commun.*, 2018, **54**, 9182–9185.
55 C. A. Goodwin, D. Reta, F. Ortu, N. F. Chilton and D. P. Mills, *J. Am. Chem. Soc.*, 2017, **139**, 18714–18724.
56 P. Evans, D. Reta, G. F. Whitehead, N. F. Chilton and D. P. Mills, *J. Am. Chem. Soc.*, 2019, **141**, 19935–19940.
57 A. Ullah, J. Cerdá, J. J. Baldovi, S. A. Varganov, J. Aragó and A. Gaita-Arino, *J. Phys. Chem. Lett.*, 2019, **10**, 7678–7683.
58 M. Amoza, L. Maxwell, N. Aliaga-Alcalde, S. Gómez-Coca and E. Ruiz, *Chem.–Eur. J.*, 2021, **27**, 16440–16447.
59 J.-L. Liu, Y.-C. Chen, Y.-Z. Zheng, W.-Q. Lin, L. Ungur, W. Wernsdorfer, L. F. Chibotaru and M.-L. Tong, *Chem. Sci.*, 2013, **4**, 3310–3316.
60 Y. C. Chen, J. L. Liu, Y. Lan, Z. Q. Zhong, A. Mansikkamaki, L. Ungur, Q. W. Li, J. H. Jia, L. F. Chibotaru, J. B. Han, W. Wernsdorfer, X. M. Chen and M. L. Tong, *Chem.–Eur. J.*, 2017, **23**, 5708–5715.
61 A. B. Canaj, M. K. Singh, C. Wilson, G. Rajaraman and M. Murrie, *Chem. Commun.*, 2018, **54**, 8273–8276.
62 A. B. Canaj, S. Dey, C. Wilson, O. Cespedes, G. Rajaraman and M. Murrie, *Chem. Commun.*, 2020, **56**, 12037–12040.
63 A. Sarkar and G. Rajaraman, *Chem. Sci.*, 2020, **11**, 10324–10330.
64 Y.-S. Ding, K.-X. Yu, D. Reta, F. Ortu, R. E. Winpenny, Y.-Z. Zheng and N. F. Chilton, *Nat. Commun.*, 2018, **9**, 3134.
65 Z.-H. Li, Y.-Q. Zhai, W.-P. Chen, Q.-C. Luo, T. Han and Y.-Z. Zheng, *Inorg. Chem. Front.*, 2020, **7**, 4367–4376.
66 P. Kalita, N. Ahmed, A. K. Bar, S. Dey, A. Jana, G. Rajaraman, J.-P. Sutter and V. Chandrasekhar, *Inorg. Chem.*, 2020, **59**, 6603–6612.
67 I. F. Díaz-Ortega, J. M. Herrera, S. Dey, H. Nojiri, G. Rajaraman and E. Colacio, *Inorg. Chem. Front.*, 2020, **7**, 689–699.
68 M. S. Norre, C. Gao, S. Dey, S. K. Gupta, A. Borah, R. Murugavel, G. Rajaraman and J. Overgaard, *Inorg. Chem.*, 2020, **59**, 717–729.
69 A. K. Bar, P. Kalita, J.-P. Sutter and V. Chandrasekhar, *Inorg. Chem.*, 2018, **57**, 2398–2401.
70 S. K. Gupta, S. Dey, T. Rajeshkumar, G. Rajaraman and R. Murugavel, *Chem.–Eur. J.*, 2022, **28**, e202103585.
71 K.-X. Yu, J. G. Kragskow, Y.-S. Ding, Y.-Q. Zhai, D. Reta, N. F. Chilton and Y.-Z. Zheng, *Chem*, 2020, **6**, 1777–1793.
72 F. Ortu, D. Reta, Y.-S. Ding, C. A. Goodwin, M. P. Gregson, E. J. McInnes, R. E. Winpenny, Y.-Z. Zheng, S. T. Liddle and D. P. Mills, *Dalton Trans.*, 2019, **48**, 8541–8545.

73 A. B. Canaj, S. Dey, C. Wilson, O. Céspedes, G. Rajaraman and M. Murrie, *Chem. Commun.*, 2020, **56**, 12037–12040.
74 A. L. Blockmon, A. Ullah, K. D. Hughey, Y. Duan, K. R. O'Neal, M. Ozerov, J. J. Baldoví, J. Aragó, A. Gaita-Ariño and E. Coronado, *Inorg. Chem.*, 2021, **60**, 14096–14104.
75 **https://cccbdb.nist.gov/vsfx.asp**.
76 J. G. Kragskow, J. Marbey, C. D. Buch, J. Nehrkorn, M. Ozerov, S. Piligkos, S. Hill and N. F. Chilton, *Nat. Commun.*, 2022, **13**, 825.
77 L. Zhu, Y. Dong, B. Yin, P. Ma and D. Li, *Dalton Trans.*, 2021, **50**, 12607–12618.
78 L. Tesi, Z. Salman, I. Cimatti, F. Pointillart, K. Bernot, M. Mannini and R. Sessoli, *Chem. Commun.*, 2018, **54**, 7826–7829.
79 A. Zabala-Lekuona, J. M. Seco and E. Colacio, *Coord. Chem. Rev.*, 2021, **441**, 213984.
80 G. Huang, X. Yi, J. Jung, O. Guillou, O. Cador, F. Pointillart, B. Le Guennic and K. Bernot, *Eur. J. Inorg. Chem.*, 2018, **2018**, 326–332.
81 H. Wada, S. Ooka, T. Yamamura and T. Kajiwara, *Inorg. Chem.*, 2017, **56**, 147–155.
82 L. Maxwell, M. Amoza and E. Ruiz, *Inorg. Chem.*, 2018, **57**, 13225–13234.
83 A. Borah, S. Dey, S. K. Gupta, G. Rajaraman and R. Murugavel, *Dalton Trans.*, 2023, **52**, 8943–8955.
84 S. K. Gupta, S. Dey, T. Rajeshkumar, G. Rajaraman and R. Murugavel, *Chem.–Eur. J.*, 2022, **28**, e202103585.
85 A. Lunghi and S. Sanvito, *Nat. Rev. Chem*, 2022, **6**, 761–781.
86 S. Mondal and A. Lunghi, *arXiv*, 2022, preprint, arXiv:2212.11705, DOI: **10.48550/arXiv.2212.11705**.
87 A. Lunghi, *arXiv*, 2022, preprint, arXiv:2202.03776, DOI: **10.48550/arXiv.2202.03776**.
88 L. Escalera-Moreno, N. Suaud, A. Gaita-Arino and E. Coronado, *J. Phys. Chem. Lett.*, 2017, **8**, 1695–1700.
89 D. López-Alcalá, A. M. Ruiz and J. J. Baldoví, *Nanomater.*, 2023, **13**, 1172.
90 R. Murugavel, S. K. Gupta, S. Dey, T. Rajeshkumar and G. Rajaraman, *Chem.–Eur. J.*, 2021, **27**, 1–12.
91 M. J. Frisch, G. W. Trucks, H. B. Schlegel, G. E. Scuseria, M. A. Robb, J. R. Cheeseman, G. Scalmani, V. Barone, B. Mennucci, G. A. Petersson, H. Nakatsuji, M. Caricato, X. Li, H. P. Hratchian, A. F. Izmaylov, J. Bloino, G. Zheng, J. L. Sonnenberg, M. Hada, M. Ehara, K. Toyota, R. Fukuda, J. Hasegawa, M. Ishida, T. Nakajima, Y. Honda, O. Kitao, H. Nakai, T. Vreven, J. A. Montgomery Jr, J. E. Peralta, F. Ogliaro, M. Bearpark, J. J. Heyd, E. Brothers, K. N. Kudin, V. N. Staroverov, R. Kobayashi, J. Normand, K. Raghavachari, A. Rendell, J. C. Burant, S. S. Iyengar, J. Tomasi, M. Cossi, N. Rega, J. M. Millam, M. Klene, J. E. Knox, J. B. Cross, V. Bakken, C. Adamo, J. Jaramillo, R. Gomperts, R. E. Stratmann, O. Yazyev, A. J. Austin, R. Cammi, C. Pomelli, J. W. Ochterski, R. L. Martin, K. Morokuma, V. G. Zakrzewski, G. A. Voth, P. Salvador, J. J. Dannenberg, S. Dapprich, A. D. Daniels, O. Farkas, J. B. Foresman, J. V. Ortiz, J. Cioslowski and D. J. Fox, *Gaussian 09, Revision A.02*, Gaussian, Inc., Wallingford CT, 2009.
92 A. D. Becke, *J. Chem. Phys.*, 1993, **98**, 5648–5652.
93 S. Grimme, J. Antony, S. Ehrlich and H. Krieg, *J. Chem. Phys.*, 2010, **132**, 154104.
94 S. Grimme, *J. Comput. Chem.*, 2006, **27**, 1787–1799.
95 X. Cao and M. Dolg, *J. Mol. Struct.: THEOCHEM*, 2002, **581**, 139–147.
96 X. Cao, *J. Chem. Phys.*, 2001, **115**, 7348.
97 V. A. Rassolov, J. A. Pople, M. A. Ratner and T. L. Windus, *J. Chem. Phys.*, 1998, **109**, 1223–1229.
98 A. Schäfer, H. Horn and R. Ahlrichs, *J. Chem. Phys.*, 1992, **97**, 2571–2577.
99 F. Aquilante, J. Autschbach, R. K. Carlson, L. F. Chibotaru, M. G. Delcey, L. De Vico, I. F. Galván, N. Ferré, L. M. Frutos and L. Gagliardi, *J. Comput. Chem.*, 2016, **37**, 506–541.
100 M. Reiher, *Theor. Chem. Acc.*, 2006, **116**, 241–252.
101 F. Aquilante, P.-Å. Malmqvist, T. B. Pedersen, A. Ghosh and B. O. Roos, *J. Chem. Theory Comput.*, 2008, **4**, 694–702.